Science Advances

AAAS

advances.sciencemag.org/cgi/content/full/3/10/eaao0713/DC1

Supplementary Materials for

Transforming from planar to three-dimensional lithium with flowable interphase for solid lithium metal batteries

Yayuan Liu, Dingchang Lin, Yang Jin, Kai Liu, Xinyong Tao, Qiuhong Zhang, Xiaokun Zhang, Yi Cui

Published 20 October 2017, *Sci. Adv.* **3**, eaao0713 (2017)
DOI: 10.1126/sciadv.aao0713

This PDF file includes:

- fig. S1. Fabrication of the 3D porous Li-rGO composite anode.
- fig. S2. SEM images of the bulk CPE.
- fig. S3. Ionic conductivities at different temperatures and photo images of PEG-LiTFSI with varying [EO]/[Li] ratios.
- fig. S4. Rheological properties of flowable PEG.
- fig. S5. Porosity of the 3D porous Li-rGO anode.
- fig. S6. Specific capacity of the 3D porous Li-rGO anode.
- fig. S7. Cross-sectional SEM images of the 3D porous Li-rGO anode with different thickness.
- fig. S8. Comparison of the exchange currents of Li foil and Li-rGO.
- fig. S9. FIB/SEM images of Li foil and 3D Li-rGO electrode after cycling.
- fig. S10. The effect of flowable interphase.
- fig. S11. The effect of high–surface area Li.
- fig. S12. Electrochemical impedance study.
- fig. S13. Symmetric cell voltage profiles at 80°C.
- fig. S14. Cycling stability of symmetric cells at 80°C.
- fig. S15. Voltage profiles of Li-LFP full cells after cycling.
- fig. S16. Cycling stability of Li-LFP cells at 80°C.
- fig. S17. Coulombic efficiency of Li-LFP cells.
- fig. S18. The electrochemical performance of Li-LFP full cells at 40°C.
- fig. S19. The electrochemical performance of symmetric cells with PEGDA middle layer at room temperature.
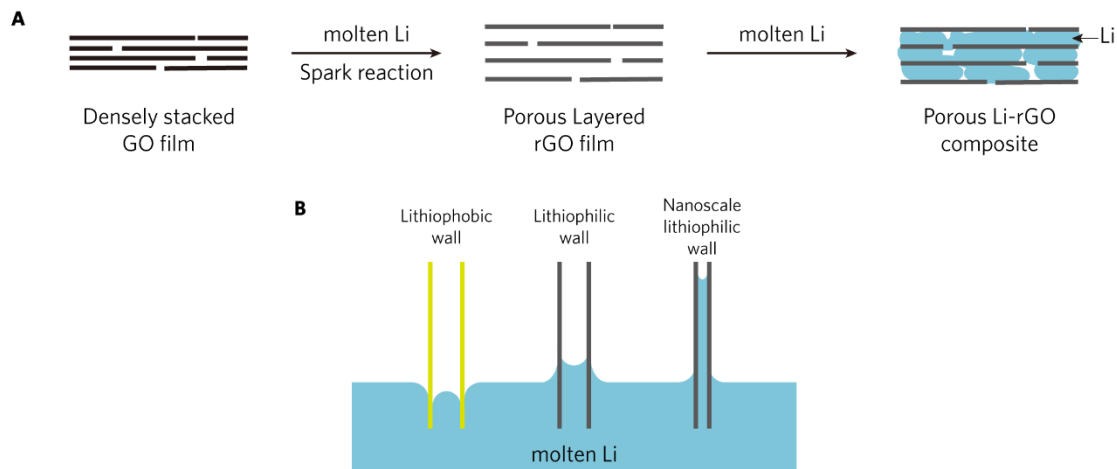- fig. S20. Characterizations on the LLZTO membranes.

fig. S1. Fabrication of the 3D porous Li-rGO composite anode. (**A**) Schematic illustration of the fabrication process of the porous Li-rGO composite electrode. Starting with densely stacked GO film, the "spark reaction" in the presence of molten Li expanded and partially reduced the GO film into a more porous layered rGO host. When the porous layered rGO film was put into contact again with molten Li, Li can be draw into the host matrix rapidly to form the porous Li-rGO composite. (**B**) Schematic illustrating the mechanism of molten Li infusion into the porous layered rGO film. The strong interaction between Li and the remaining oxygen-containing surface functional groups of rGO results in a lithiophilic surface (good wettability by molten Li). It is known that the capillary force on a poor wetting surface will lower the liquid level while a good wetting surface will raise the liquid level. The height of the liquid level is inversely proportional to the dimension of the gaps. Therefore, the nanoscale gaps between the rGO layers can provide strong capillary force to drive the molten Li intake into the rGO host. Due to the importance of the capillary force between the nanoscale gaps, the surface of the Li-rGO composite is not covered with thick metallic Li.
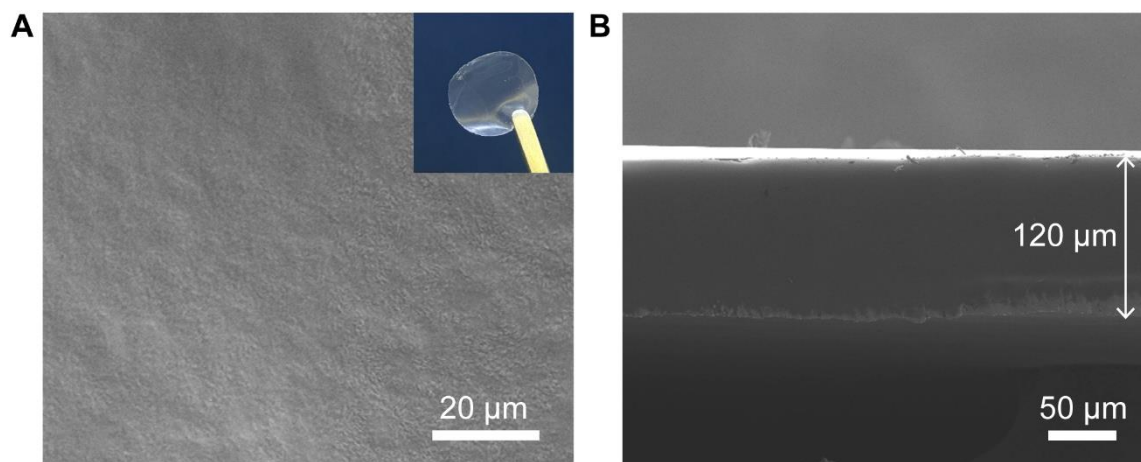
fig. S2. SEM images of the bulk CPE. (**A**) Top and (**B**) cross sectional SEM images of the bulk CPE used in the study. Figure (**A**) inset is the digital photo image of the bulk CPE.
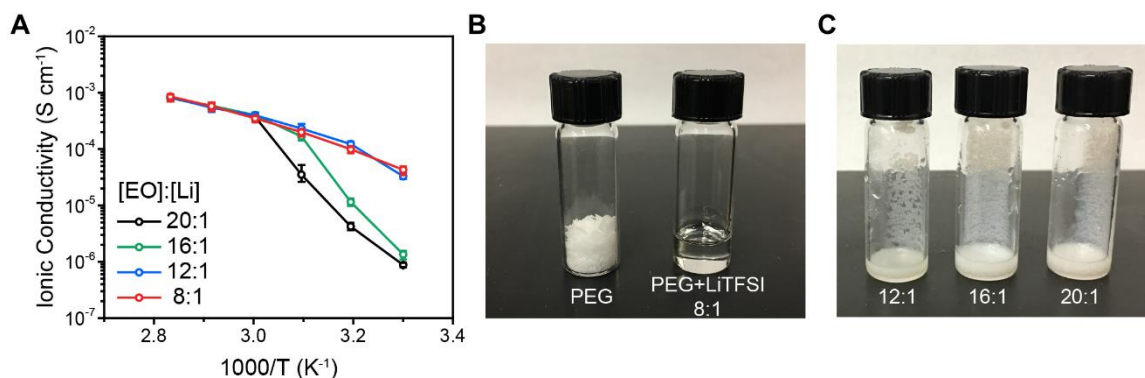

fig. S3. Ionic conductivities at different temperatures and photo images of PEG-LiTFSI with varying [EO]/[Li] ratios. (**A**) Ionic conductivity of PEG-LiTFSI at different temperatures with varying [EO] to [Li] ratios. (**B, C**) Photo images of pure PEG and PEG-LiTFSI at varying [EO] to [Li] ratios at room temperature. The liquid-like state of PEG-LiTFSI becomes more stable at room temperature as the concentration of LiTFSI increases. The 8 to 1 ratio was selected in this study to give a flowable PEG even at room temperature and high ionic conductivity over a wide temperature range.
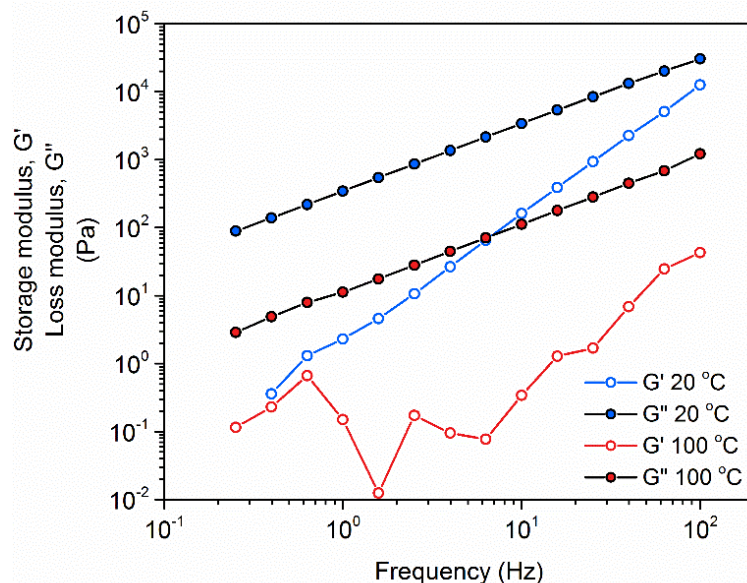
fig. S4. Rheological properties of flowable PEG. Storage modulus (G') and loss modulus (G") of the flowable PEG electrolyte measured at 20ºC and 100ºC.
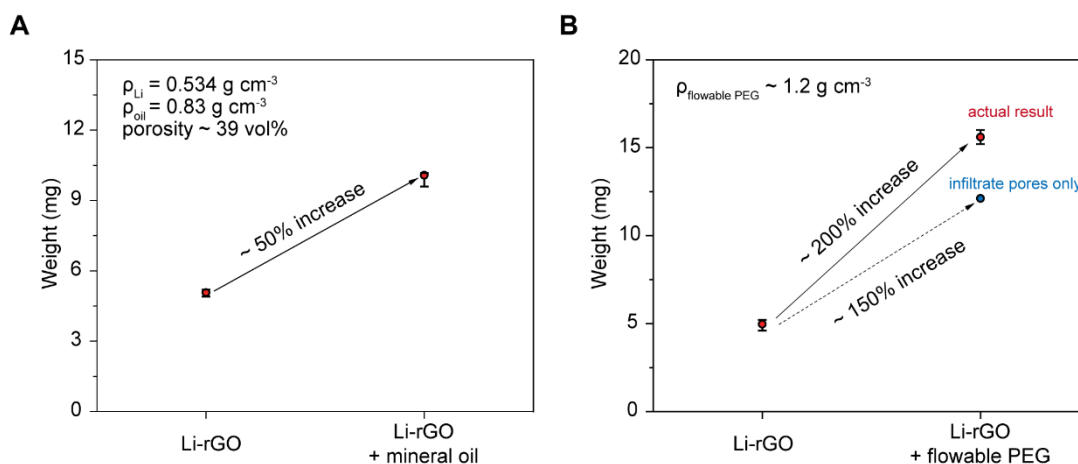

fig. S5. Porosity of the 3D porous Li-rGO anode. (**A**) The porosity of the 3D Li-rGO anode measured by mineral oil absorption, which resulted in a value of ~ 39 vol% for electrodes typically used in this study. The weight of the electrode was ~ 5 mg cm^{-2}. (**B**) The weight increase of the 3D Li-rGO anode after flowable PEG electrolyte infiltration (~ 200% increase, red dot). Given the density of the flowable PEG electrolyte (~1.2 g cm^{-3}), the theoretical weight increase of the electrode with 39 vol% porosity if completely infiltrated by the electrolyte is ~ 150% (blue dot). In addition, there was also a thin layer of flowable PEG covering the surface of Li-rGO, and thus, the measured value is reasonable.
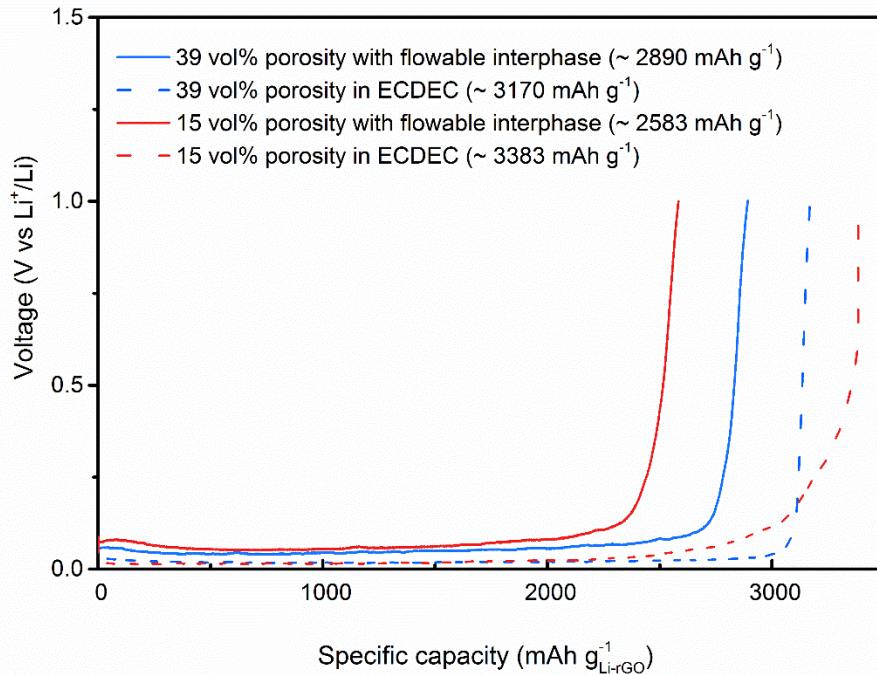
fig. S6. Specific capacity of the 3D porous Li-rGO anode. Li stripping curve of the Li–rGO electrodes with two different porosities (39 vol% and 15 vol%) in both liquid electrolyte (ECDEC) and solid-state cells with flowable interphase. Higher capacity could be extracted in solid-state cells as the porosity of the Li-rGO increased.
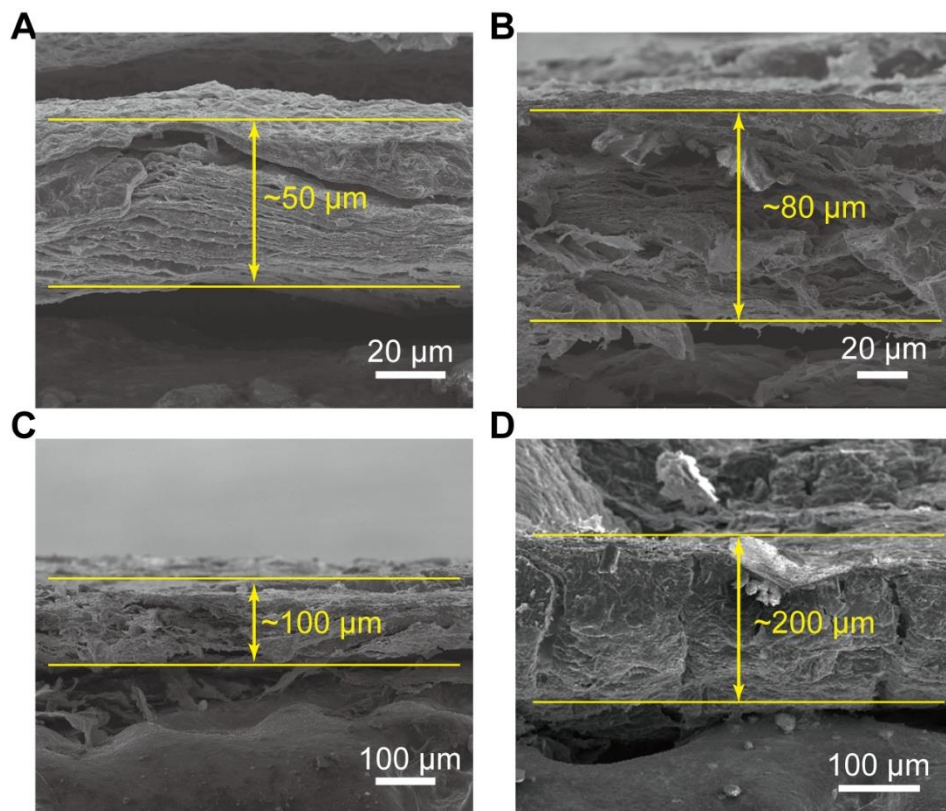
fig. S7. Cross-sectional SEM images of the 3D porous Li-rGO anode with different thickness. The thickness can be easily tuned by varying the thickness of the starting GO film so as to tune the mass loading of the Li anode.
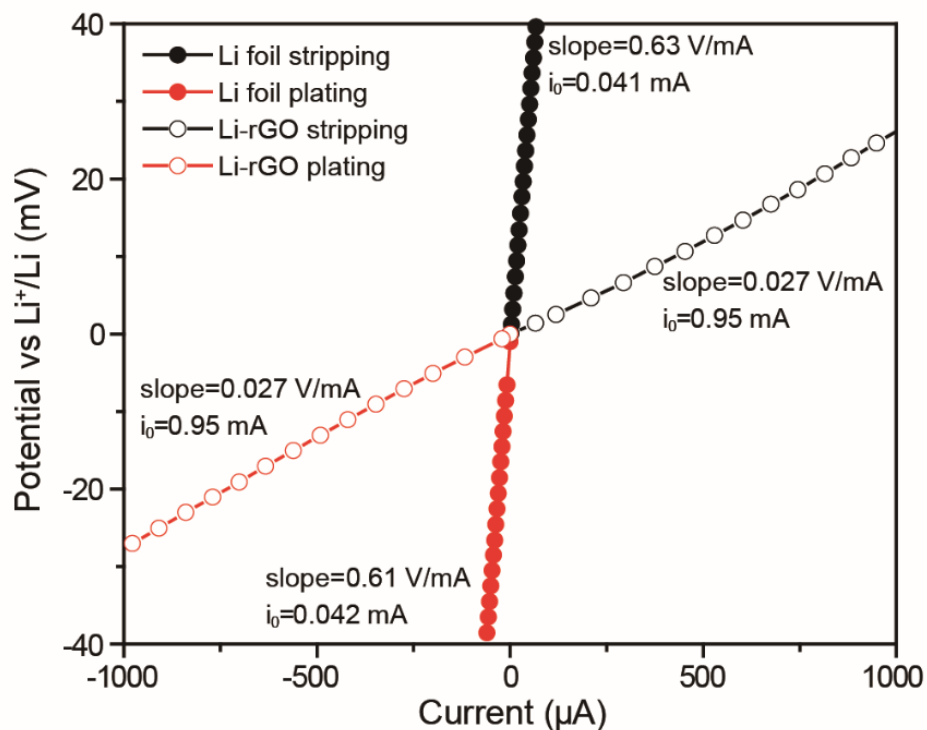
fig. S8. Comparison of the exchange currents of Li foil and Li-rGO. The difference in exchange current density should be comparable to the difference in electroactive surface area. Exchange current density reflects the intrinsic rate of electron transfer between the electrode and the electrolyte. Under the same electrochemical environment, the intrinsic Li stripping/plating rate shall be the same for both Li foil electrode and the 3D Li-rGO electrode. Nevertheless, the electroactive surface area of 3D Li-rGO is much larger than its geometric area, resulting in much greater apparent exchange current density than that of the planar Li foil. The exchange current density of Li-rGO is over 20 times the value of Li foil. Thus, the electroactive surface area of Li-rGO can be approximated as at least one order of magnitude larger, which can reduce the interfacial fluctuation from tens of microns to submicron scale.
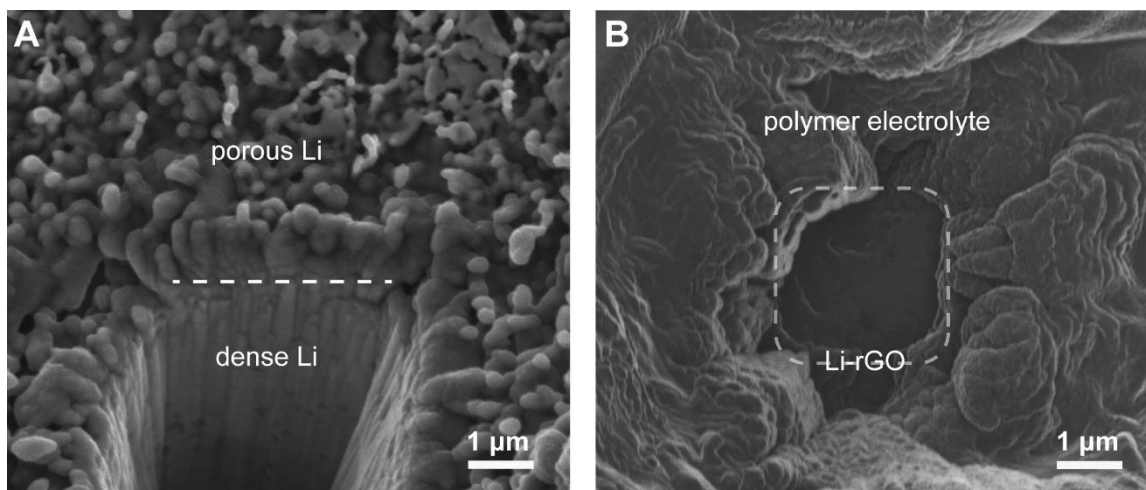
fig. S9. FIB/SEM images of Li foil and 3D Li-rGO electrode after cycling. (**A**) Li foil and (**B**) 3D Li-rGO electrode after 50 cycles of symmetric cell cycling at a current density of 0.2 mA cm^{-2}, a cycling capacity of 0.2 mAh cm^{-2} and a temperature of 60°C. The surface of the Li foil was porous and rough after cycling, under which dense Li can be observed after FIB milling. On the other hand, after the residual polymer electrolyte on the surface of the Li-rGO electrode was milled away (milling area delineated by dash line), the underlying electrode appeared relatively smooth.
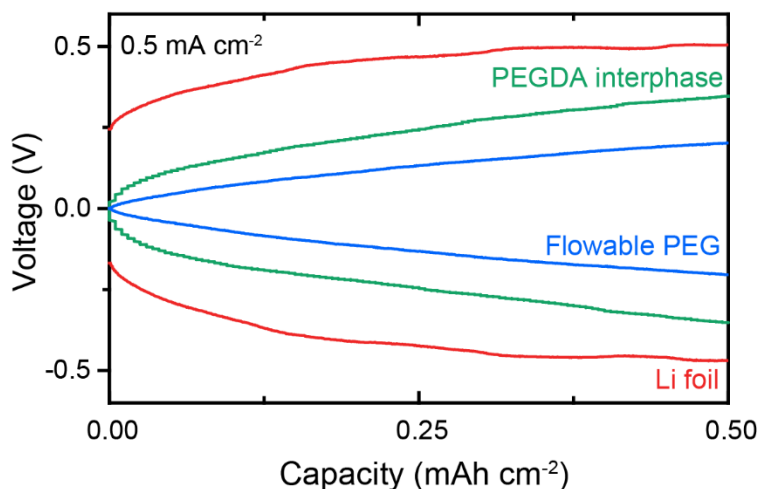

fig. S10. The effect of flowable interphase. Voltage profiles of Li foil (red), 3D Li-rGO with relatively rigid PEGDA interphase (green) and 3D Li-rGO with flowable PEG interphase (blue) at a current density of 0.5 mA cm^{-2} and a temperature of 60°C. CPE was used as the bulk solid electrolyte.
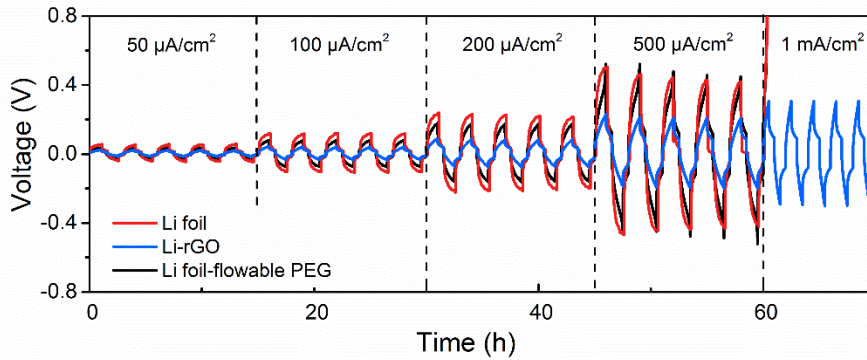
fig. S11. The effect of high–surface area Li. Galvanostatic cycling of symmetric cells using 3D Li-rGO with flowable interphase (blue), bare Li foil (red) and Li foil with 10 μL flowable PEG on the surface (black) at 60°C with different current densities. CPE was used as the bulk solid electrolyte.

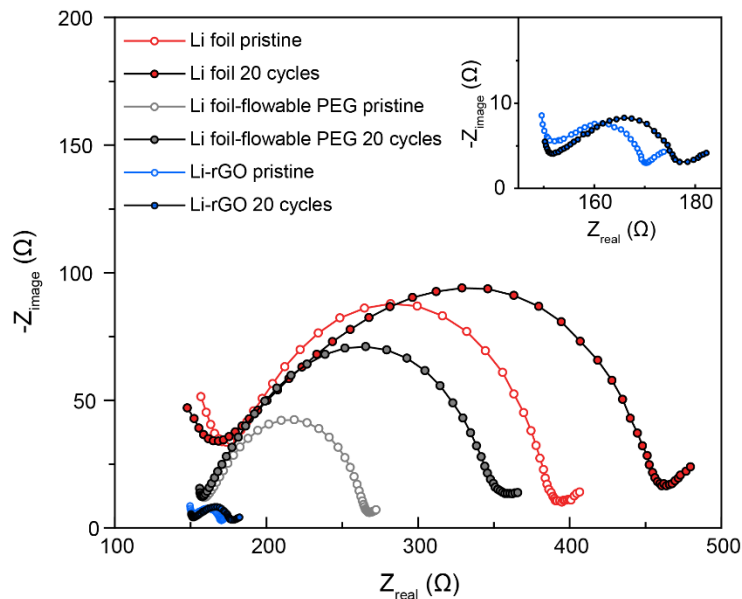**fig. S12. Electrochemical impedance study.** Nyquist plots of symmetric cells with bare Li foil, Li foil with 10 μL flowable PEG on the surface and 3D porous Li-rGO electrodes before and after 20 galvanostatic cycles at a current density of 0.2 mA cm^{-2}, a cycling capacity of 0.2 mAh cm^{-2} and an operating temperature of 60°C. CPE was used as the bulk solid electrolyte and the measurements were also carried out at 60°C.

fig. S13. Symmetric cell voltage profiles at 80°C. (**A**) Galvanostatic cycling of symmetric cells using 3D Li-rGO electrodes with flowable interphase and planar Li foil electrodes at 80ºC with different current densities. The charging and discharging time was fixed at 1 hr with 30 min rest in between. (**B** to **E**) are the detailed voltage profiles at a current density of 100 μA cm⁻², 200 μA cm⁻², 500 μA cm⁻² and 1 mA cm⁻², respectively. CPE was used as the bulk solid electrolyte.
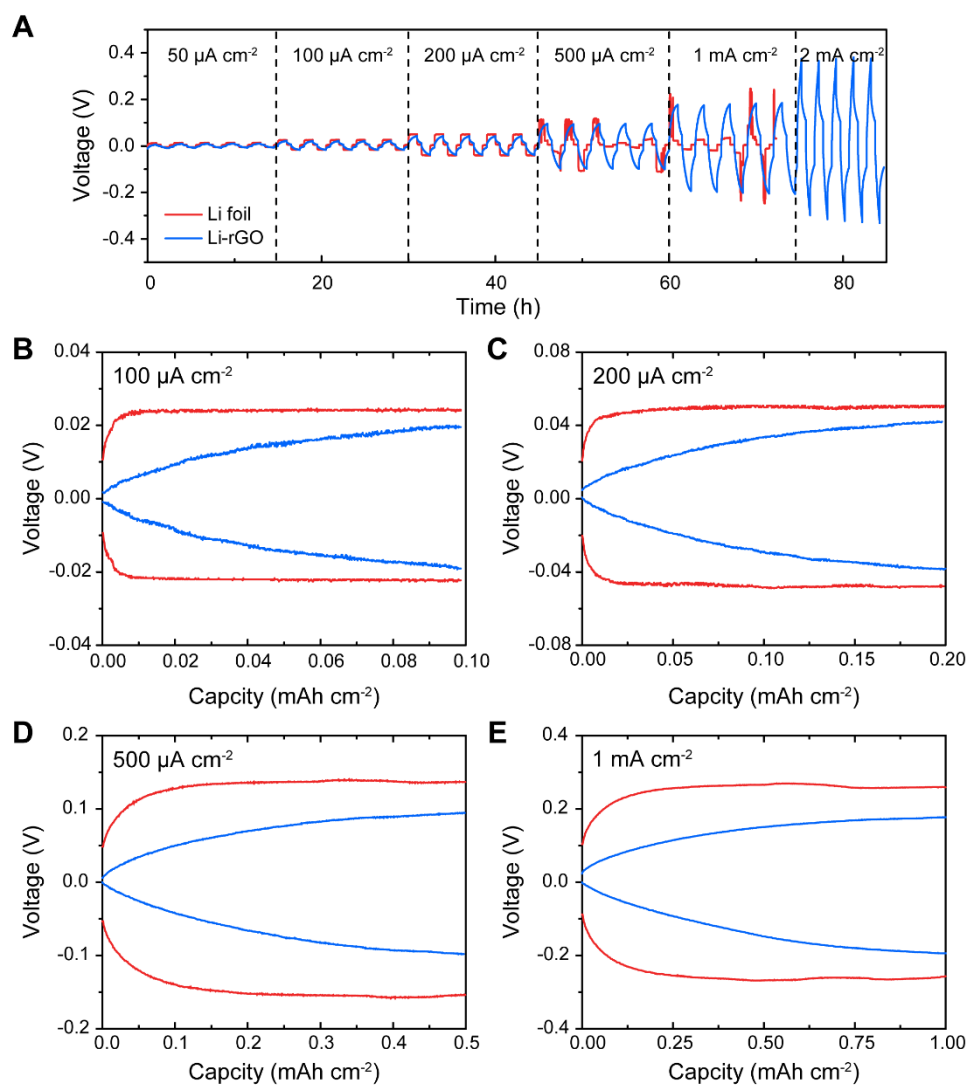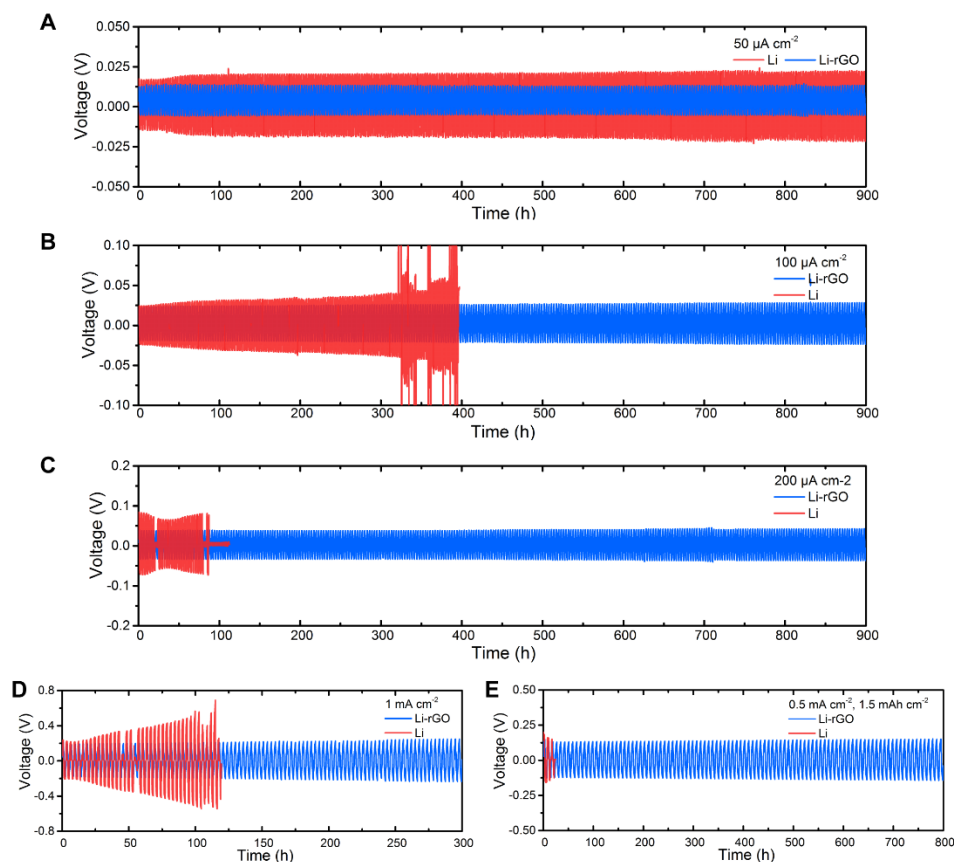
fig. S14. Cycling stability of symmetric cells at 80°C. Long-term galvanostatic cycling of symmetric cells using 3D Li-rGO electrodes with flowable interphase and planar Li foil electrodes at 80°C at a current density of (**A**) 0.05 mA cm^{-2}, (**B**) 0.1 mA cm^{-2}, (**C**) 0.2 mA cm^{-2} and (**D**) 1 mA cm^{-2}, respectively. The charging and discharging time was fixed at 1 hr with 30 min rest in between. (**E**) Galvanostatic cycling of the symmetric cells at a current density of 0.5 mA cm^{-2} and a cycling capacity of 1.5 mAh cm^{-2}. The cells were rested for 1 hr between each charging and discharging cycle. CPE was used as the bulk solid electrolyte.
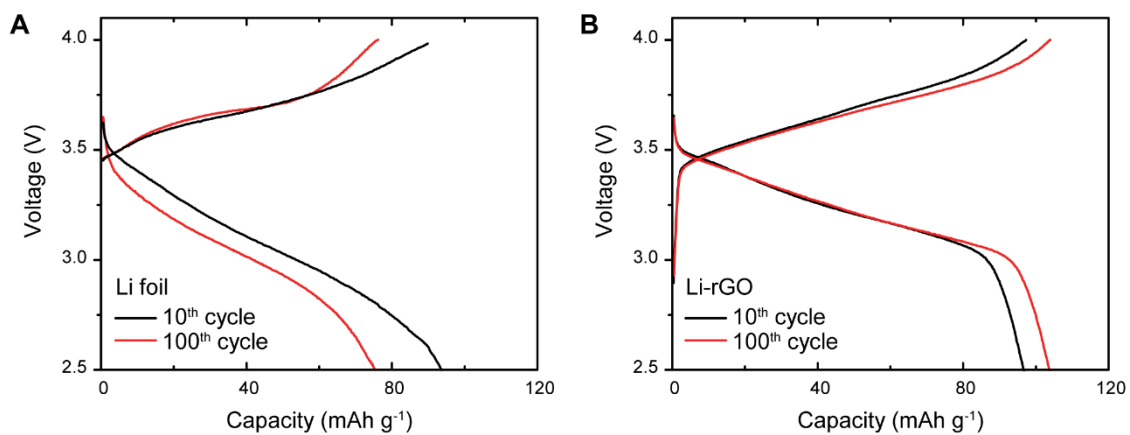
fig. S15. Voltage profiles of Li-LFP full cells after cycling. Galvanostatic charge/discharge voltage profiles of Li-LFP full cells at the 10th and the 100th cycle using (**A**) Li foil and (**B**) 3D Li-rGO as the anode at a current density of 1 mA cm^{-2} and an operation temperature of 60°C. CPE was used as the bulk solid electrolyte.
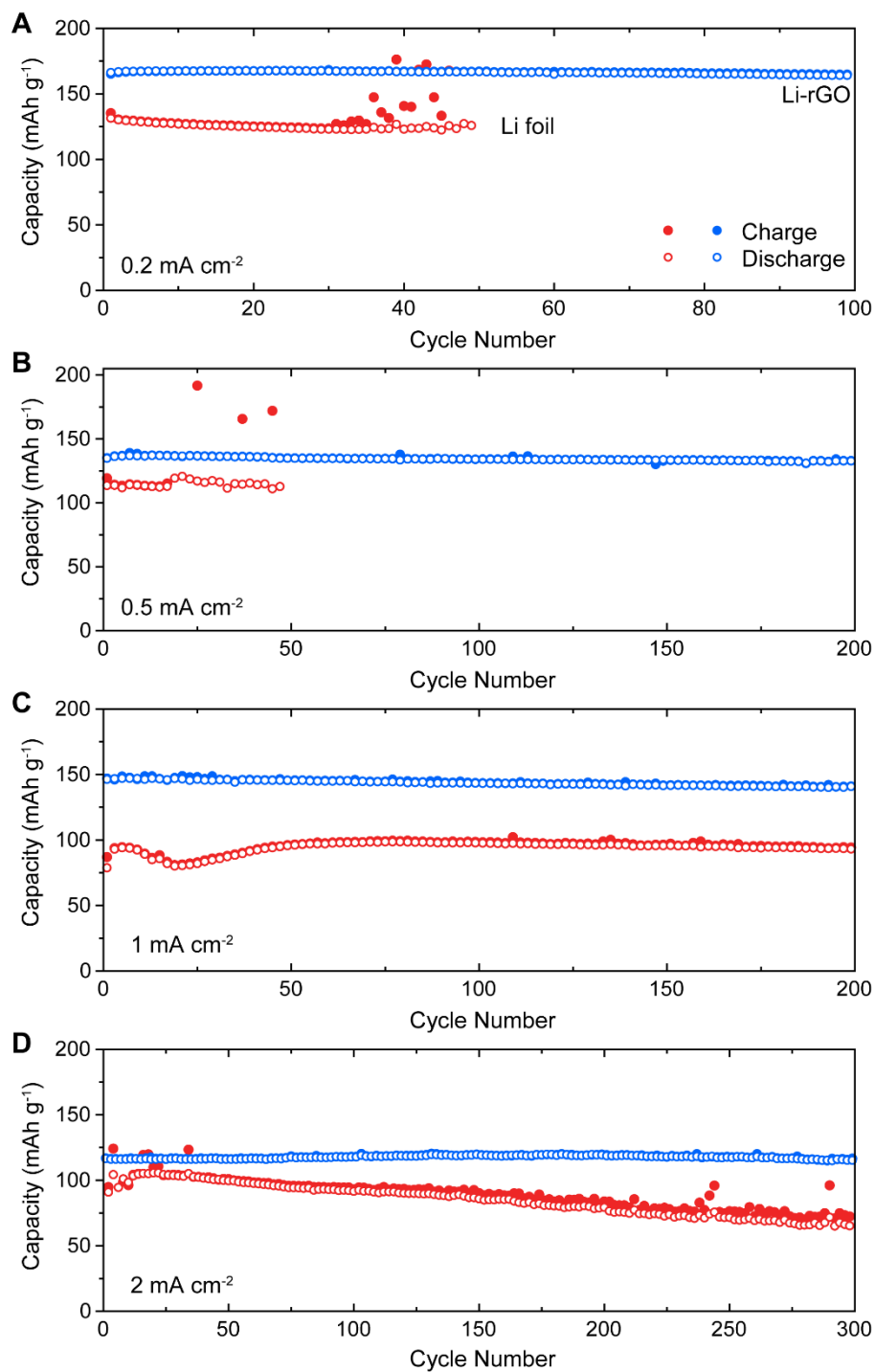
fig. S16. Cycling stability of Li-LFP cells at 80°C. Long-term cycling performance of solid-state Li-LFP batteries using either Li foil or 3D Li-rGO anode at an operation temperature of 80°C and a current density of (**A**) 0.2 mA cm^{-2}, (**B**) 0.5 mA cm^{-2}, (**C**) 1 mA cm^{-2}, and (**D**) 2 mA cm^{-2}, respectively. The scattered charge/discharge values of the Li foil cells indicate the occurrence of soft internal short circuits. CPE was used as the bulk solid electrolyte.
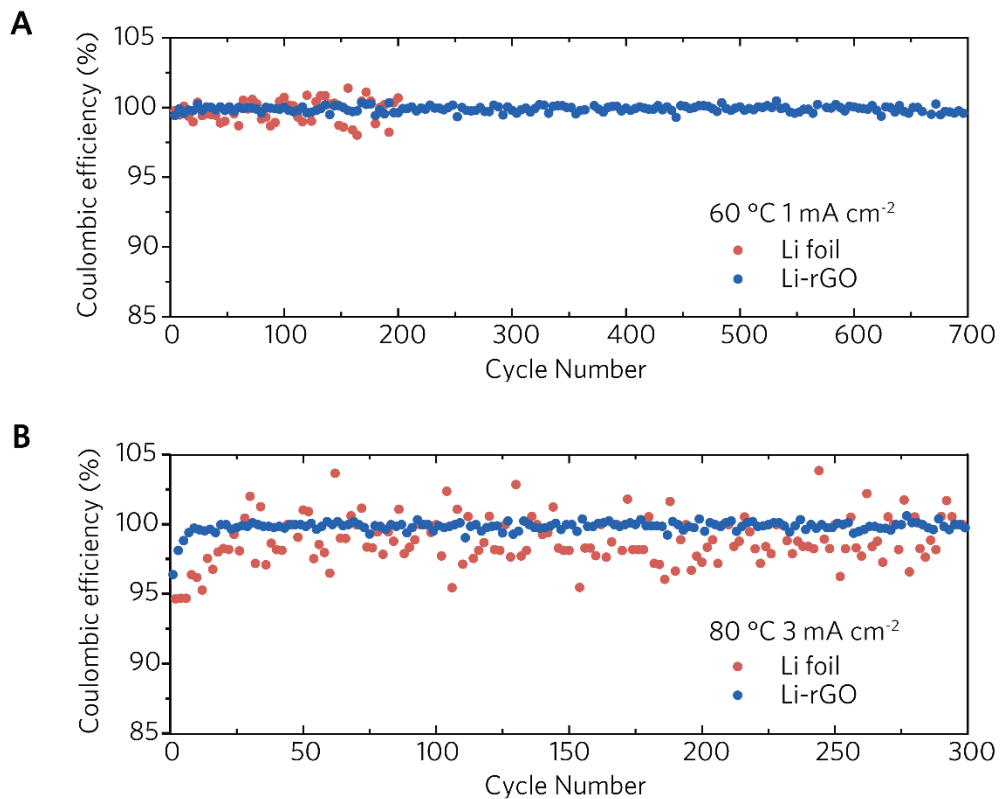
fig. S17. Coulombic efficiency of Li-LFP cells. The Coulombic efficiency data of solid-state Li-LFP batteries using either Li foil or 3D Li-rGO anode cycled at (**A**) 1 mA cm^{-2} at 60°C (corresponding to Fig. 4D) and (**B**) 3 mA cm^{-2} at 80°C (corresponding to Fig. 4H). CPE was used as the bulk solid electrolyte. The Coulombic efficiency of the 3D Li-rGO cells was stable, approaching 100% while the Coulombic efficiency of the Li foil cells was much lower and much more scattered.
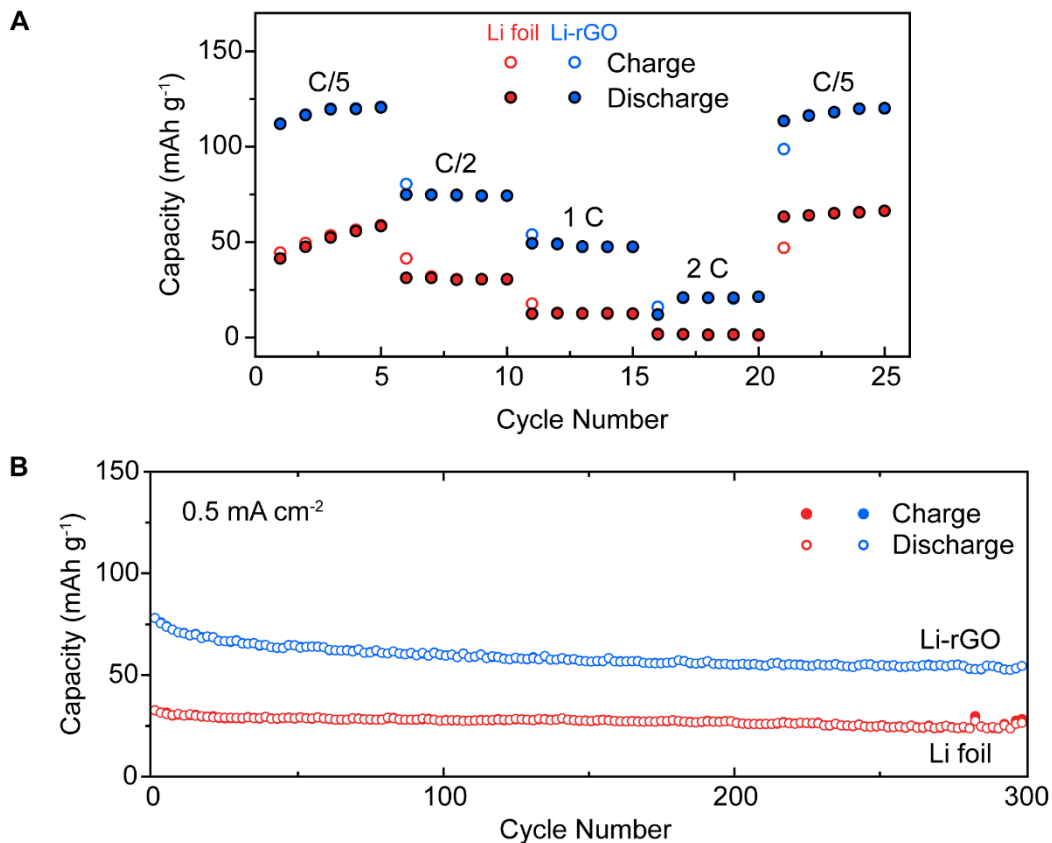
fig. S18. The electrochemical performance of Li-LFP full cells at 40°C. (**A**) Rate capability of Li-LFP full cells using either 3D Li-rGO or Li foil as the anode at an operation temperature of 40°C. (**B**) Long-term cycling performance of solid-state Li-LFP batteries using either Li foil or 3D Li-rGO anode at an operation temperature of 40°C and a current density of 0.5 mA cm^{-2}. CPE was used as the bulk solid electrolyte.
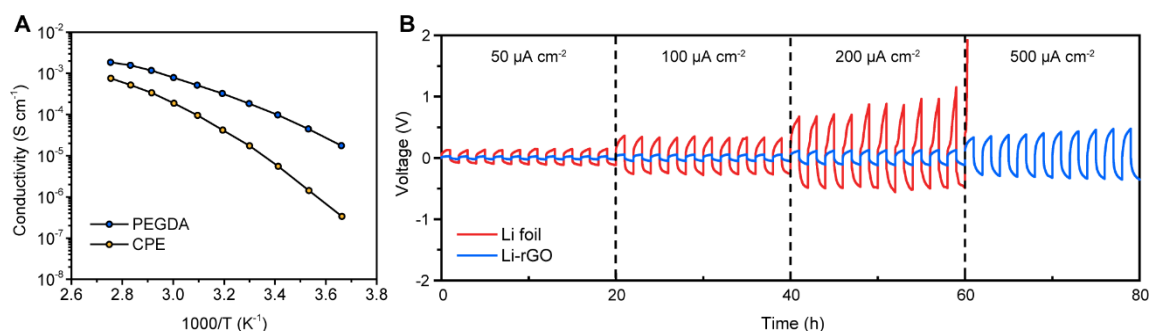
fig. S19. The electrochemical performance of symmetric cells with PEGDA middle layer at room temperature. (**A**) Ionic conductivity of the crosslinked PEGDA solid electrolyte. (**B**) Galvanostatic cycling of symmetric cells using 3D Li-rGO electrodes with flowable interphase and planar Li foil electrodes at room temperature using the crosslinked PEGDA as the middle layer. The charging and discharging time was fixed at 1 hr.

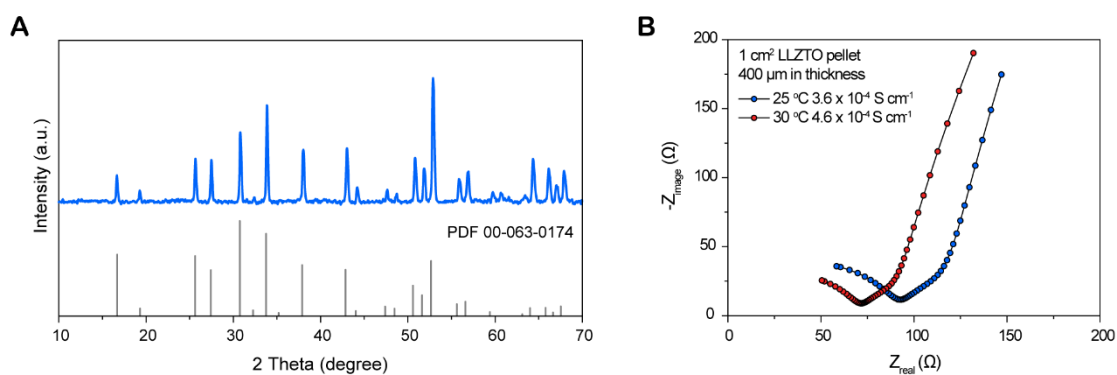**fig. S20. Characterizations on the LLZTO membranes.** (**A**) X-ray diffraction pattern of the as-prepared LLZTO ceramic solid electrolyte membrane and the standard cubic garnet $Li_7La_3Zr_2O_{12}$ (PDF #00-063-0174). (**B**) Impedance spectra of a 400 μm LLZTO membrane at 25°C and 30°C, from which the ionic conductivity value was calculated to be 3.6 x 10^{-4} and 4.6 x 10^{-4} S cm^{-1}, respectively.

Supplementary Table

table S1. Comparison of the electrochemical performance of our solid-state Li battery using 3D Li with flowable interphase with those reported in the literature using the Li foil anode.

	Solid electrolyte	**Cathode (capacity)**	**Current Density**	**Performance**	**Temperature (°C)**	*Ref. (year)*
Planar Li foil	PEO plasticized by tetraglyme	TiO_2 (unknown)	0.1 mA cm^{-2}	130 mAh g^{-1}	20	*21* (2016)
	PEO + super acid ZrO_2	LFP (1 mAh cm^{-2})	C/7	150 mAh g^{-1} 100 mAh g^{-1}	90 75	*44* (2006)
	PEO + ZrO_2	LFP (0.5 mAh cm^{-2})	1 C	60 mAh g^{-1}	100	*45* (2010)
	Block copolymer PS-b-PEO	LFP (0.6 mAh cm^{-2})	0.28 C	140 mAh g^{-1}	90	*46* (2013)
	Triblock copolymer P(STFSILi)-b-PEO-b-P(STFSILi)	LFP (0.8 mAh cm^{-2})	1 C	100 mAh g^{-1}	60	*17* (2013)
	Polyhedral oligomeric silsesquioxane crosslinked PEG	LFP (unknown)	1 C 2 C	135 mAh g^{-1} 90 mAh g^{-1}	90	*47* (2015)
	PEO + *in situ* synthesized silica	LFP (0.15 mAh cm^{-2})	1 C	100 mAh g^{-1}	60	*38* (2015)
	PEO + $Li_{10}GeP_2S_{12}$	LFP (unknown)	0.88 C	99 mAh g^{-1}	60	*48* (2016)
	PEO + hollow mesoporous organic polymers	LFP (0.34 mAh cm^{-2})	1 C 2 C	108 mAh g^{-1} 85 mAh g^{-1}	65	*49* (2016)
	polymer/ceramic membrane/polymer sandwich electrolyte	LFP (0.85 mAh cm^{-2})	0.5 C	120 mAh g^{-1}	65	*23* (2016)
	LiPON/LATP	$LiNi_{1/3}Co_{1/3}Mn_{1/3}O_2$ (0.2 mAh cm^{-2})	0.025 C	152 mAh g^{-1}	60	*40* (2014)
	Li_2S-P_2S_5	2.1 V Sulfur (0.35 mAh cm^{-2})	0.05 C	400 mAh g^{-1}	80	*50* (2013)
	$Li_{10}GeP_2S_{12}$/70%Li_2S−29% P_2S_5−1% P_2O_5 bilayer	0.5–3 V Co_9S_8-$Li_7P_3S_{11}$ (1.5 mAh cm^{-2})	1.27 mA cm^{-2}	500 mAh g^{-1}	25	*51* (2016)
	$Li_7La_3Zr_2O_{12}$	$TiNb_2O_7$ (~0.07 mAh cm^{-2})	2 μA cm^{-2}	170 mAh g^{-1}	60	*41* (2016)
3D Li	**Flowable PEG + PEO**	**LFP (1 mAh cm^{-2})**	**1 C** **2 C** **5 C**	**126 mAh g^{-1}** **100 mAh g^{-1}** **70 mAh g^{-1}**	**60**	**This work**
			1 C **2 C** **5 C**	**141 mAh g^{-1}** **132 mAh g^{-1}** **110 mAh g^{-1}**	**80**	